

## Solar cities: Multiple-reflection within urban canyons

Fan Xu <sup>a</sup>, Man Sing Wong <sup>a,b,c</sup>,\*, Rui Zhu <sup>d</sup>, Ying Dang <sup>e</sup>

<sup>a</sup> Department of Land Surveying and Geo-Informatics, The Hong Kong Polytechnic University, Hung Hom, 999077, Hong Kong Special Administrative Region, China

<sup>b</sup> Research Institute for Sustainable Urban Development, The Hong Kong Polytechnic University, Hung Hom, 999077, Hong Kong Special Administrative Region, China

<sup>c</sup> Research Institute of Land and Space, The Hong Kong Polytechnic University, Hung Hom, 999077, Hong Kong Special Administrative Region, China

<sup>d</sup> Institute of High Performance Computing (IHPC), Agency for Science, Technology and Research (A\*STAR), 1 Fusionopolis Way, Singapore, 138632, Republic of Singapore

<sup>e</sup> Institute of Chinese Historical Geography, Fudan University, 220 Handan Road, Shanghai, 200433, China

### ARTICLE INFO

#### Keywords:

Façade  
Material  
Solar potential  
Albedo

### ABSTRACT

Solar photovoltaic (PV) harvesting is a significant energy resource leading to the rapid expansion of renewable energy. To facilitate decision-making regarding the optimal location and appropriate time for harvesting solar energy, the precise estimation of solar potential distribution in a city especially in 3D context is essential. However, using constant values to represent the urban vertical façades in a city and/or ignoring the indirect components under the estimation of received irradiation have been adopted in the current research, which may lead to inaccuracies in final results particular in complex urban environment. In this work, we propose a methodology to estimate the solar potential accurately by incorporating the façade albedo using street view images, as well as considering multiple reflection in urban canyon. Furthermore, this method is further integrated in the proposed evaluation framework to assess the impact of urban façade albedo on solar potential distribution. Compared to existing methods, the proposed framework first discusses and analyzes the importance of façade albedo and evaluates its impact quantitatively. The experimental results show that the discrepancies in albedo significantly affect the overall solar potential by 8.0% to 9.1%. If multiple reflections under urban canyon are disregarded, the impact can reach 11.9% to 17.8%.

### 1. Introduction

Electricity is the driving force of modern societies and economies but is also a significant emission source of carbon dioxide (CO<sub>2</sub>) worldwide. The rapid expansion of renewable energy sources, such as solar, wind power, and hydroelectricity, is spearheading the transition to net zero emissions, with the World's total renewable electricity capacity projected to rise to 4500 gigawatts (GW) by 2024 (IEA, 2023). In this context, estimating the solar photovoltaic (PV) potential distribution accurately and efficiently provides a crucial foundation for energy policy decision-making as well as the spatial optimization of solar PV harvesting (Zhu et al., 2023; Izquierdo et al., 2011).

In recent years, studies have been dedicated to improving the efficiency and accuracy of the land surface solar irradiation estimation (Gassar and Cha, 2021). Empirical models use multiple meteorological parameters, such as temperature, relative humidity, and precipitation, to describe the long-term or short-term distribution of solar potential over large areas (Chen et al., 2019; Makade et al., 2019).

However, as the number of variables increases, traditional models are not capable to reflect this complex and nonlinear relationships (Ağbulut et al., 2021). In contrast, machine learning method have been developed to explain implicit mappings when sufficient data is available (Meenal and Selvakumar, 2018; Jiang et al., 2017; Ibrahim and Khatib, 2017).

These approaches, however, have certain limitations. Firstly, the lack of incorporation of urban microclimate conditions and interactions among buildings, such as shadowing casted by buildings within urban canyon and solar multi-reflections, leads to inaccurate results (Freitas et al., 2015; Zhu et al., 2023). Secondly, neglecting the solar irradiation received by urban vertical surfaces significantly underestimates the solar PV potential in cities. Despite receiving less vertical irradiation and having a higher shadow covering rate, façades can generate more energy than rooftops due to their larger area (Redweik et al., 2013). In metropolitan cities, the high density and large ratio of façade area to roof area mean that urban morphology significantly influences the

\* Corresponding author at: Department of Land Surveying and Geo-Informatics, The Hong Kong Polytechnic University, Hung Hom, 999077, Hong Kong Special Administrative Region, China.

E-mail addresses: [fanfan.xu@connect.polyu.hk](mailto:fanfan.xu@connect.polyu.hk) (F. Xu), [ls.charles@polyu.edu.hk](mailto:ls.charles@polyu.edu.hk) (M. Wong), [zhur@ihpc.a-star.edu.sg](mailto:zhur@ihpc.a-star.edu.sg) (R. Zhu), [ydang20@fudan.edu.cn](mailto:ydang20@fudan.edu.cn) (Y. Dang).

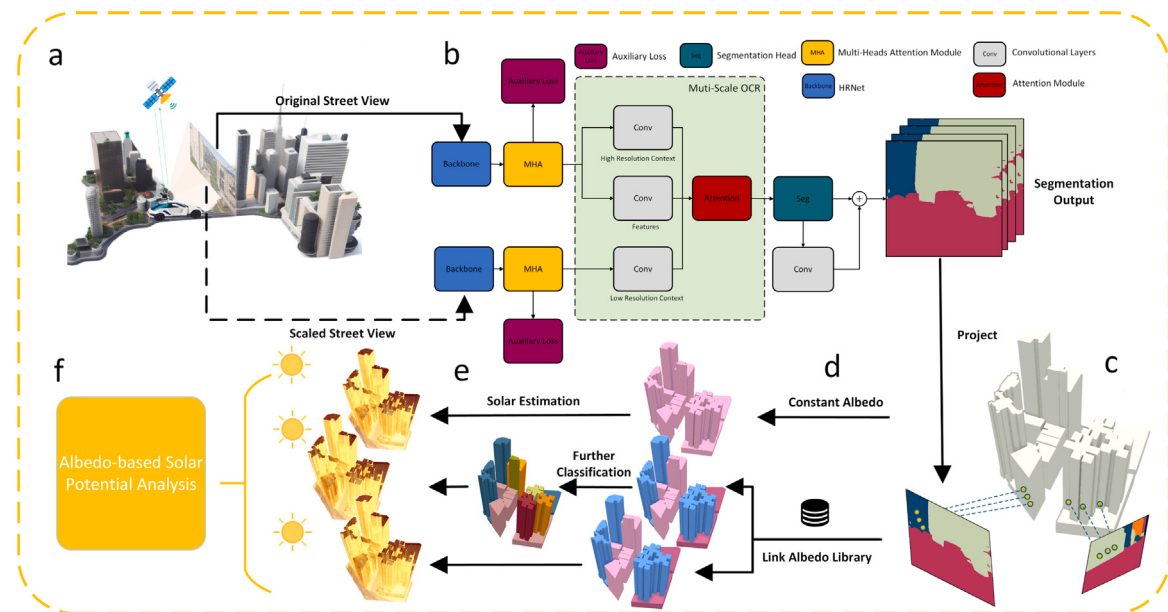


**Fig. 1.** The evaluation framework. (a) Using the vehicle-based mobile mapping system to collect street view images with geographical coordinates. (b) MSCA is utilized to identify the material categories from street views. (c) Projecting the 2D segmentation results to the 3D urban GIS model. (d) Based on three different albedo schemes, mapping the identified materials to distinct albedo: constant albedo, simulation albedo, and segmentation-based albedo. (e) Solar potential estimation based on three albedo schemes. (f) Analyzing the solar potential distributions with different albedo schemes and spatial characteristics.

distribution of solar photovoltaic potential, which is difficult to capture in two-dimensional estimation models (Walch et al., 2020; Park et al., 2021; Assouline et al., 2015, 2017).

Three-dimensional (3D) geographic information system (GIS) models have proven to be a promising approach for accurate solar analysis at the building scale (Zhu et al., 2020, 2019; Li et al., 2016; Erdélyi et al., 2014; Zhu et al., 2022). Regardless of the Level-of-Detail (LoD), 3D models can quantify building occlusion and the solar PV potential on vertical surfaces. However, due to the lack of urban envelope albedo information, inter-building reflection within canyon, a significant component of solar irradiation, has been omitted in most studies (Sánchez and Izard, 2015; Boccalatte et al., 2020). Some studies apply a constant value to represent the albedo of all urban façades (Zhu et al., 2020, 2022). Considering the diverse architectural styles in metropolitan cities, the irradiation of reflected solar light can vary significantly between districts. For instance, a rooftop near a commercial building with a high albedo glass façade likely receives higher irradiation than one near an old residential building with a mosaic tile façade (Mehaoued and Lartigue, 2019).

Accurately estimating solar potential by incorporating albedo-based multi-reflection and quantifying the effect of façade albedo on solar PV distribution is challenging due to the labor-intensive nature of collecting albedo data at a city scale. A study proposed a multi-scale contextual attention network (MSCA) to effectively identify materials from street views (Xu et al., 2023). Based on the MSCA, we proposed a comprehensive evaluation framework for investigating the effect of albedo on solar PV potential distribution. This study selected a typical urban area in Hong Kong, as the study area to collect street view images. After processing with the MSCA, the segmentation results are projected onto the 3D GIS model. According to the identified materials, each building in the study area is assigned three different albedos: constant albedo, simulation albedo, and segmentation-based albedo. The 3D building models with different albedo strategies are used to evaluate the effect on solar potential distribution. In accordance with the experimental results, this study found that the discrepancy in façade albedo strategies has a significant impact on the distribution of solar potential. Under different urban morphologies and time scales, albedo determines the distribution of irradiance to different degrees.

The new contributions of this study are listed below:

- (1) This study presents a comprehensive evaluation framework for investigating the effect of albedo on solar PV potential distribution. The proposed framework allows to acquire large-scale façade information in a complex urban environment and converts it into the format of a 3D model efficiently. This provides the essential source for precisely estimating the solar PV potential distribution. In this study, the differences caused by albedo under circumstances with diverse spatial and temporal elements are identified and evaluated in detail.
- (2) To quantify the effect of different façade materials on solar PV potential distribution, this study proposed to use specific albedo for each building to accurately estimate the multi-reflection for calculating the solar irradiation. The experiments suggested that in the selected study area, different albedo distribution strategies significantly affect the overall solar potential by 8.0% to 9.1%. If multiple reflection effects within buildings are disregarded, the impact can reach 11.9% to 17.8%.

The remainder of the paper is organized as follows. Section 2 reviews related work and current technology. Section 3 presents the materials and methods, including the data preparation and the details of our evaluation framework. In Section 4, we estimate the solar distribution and analyze the irradiation under circumstances with diverse spatial and temporal elements. Conclusions and future work are discussed in Section 5.

## 2. Related work

### 2.1. Solar potential estimation

Solar potential estimation models based on two-dimensional inputs typically can be categorized as empirical models (Chen et al., 2019; Makade et al., 2019), physical models (Nguyen and Pearce, 2013; Zhu et al., 2020), and machine learning models (Assouline et al., 2015, 2017; Nwokolo et al., 2023). Besides the common meteorological parameters (Besharat et al., 2013), like cloud cover, ambient temperature, and relative humidity, studies proposed to utilize sunshine duration or rainfall data to optimize the estimation (Quej et al., 2016; Meenal and Selvakumar, 2016). With the increasing parameters are found relevant

to the solar distribution, tradition models lack insufficient generalization ability to map independent and dependent variables. Meenal and Selvakumar (2018) propose to identify the most influencing factors by using Waikato Environment for Knowledge Analysis (WEKA) evaluating the accuracy of Support Vector Machine (SVM), Artificial Neural Network (ANN). To further improve the accuracy of solar estimation, 3D model was introduced to compute the shadow cast in rooftops (Li et al., 2016). Similarly, SORAM model used a ray-tracing algorithm to determine whether a 3D ray vector intersects with a voxel and to calculate dynamic 3D shading from urban obstacles (Erdélyi et al., 2014). Furthermore, the solar potential on vertical surface is incorporated in the computing (Xu et al., 2019; An et al., 2023; Willenborg et al., 2018b). 3D models based on technologies (e.g., LiDAR data, semantic 3D city model, and 3D mesh models) are developed for higher LoD and accuracy (Bill et al., 2016; Willenborg et al., 2018a). However, only a few estimations include the inter-building reflection (Zhu et al., 2020, 2022). In these studies, the albedo assigned to urban envelopes is a constant value, which has resulted in imprecise results, and the effect is challenging to quantify.

## 2.2. Albedo determination

Building integrated photovoltaic (BIPV) on façades is sensitive to the variations of the solar indirect components (i.e., multi-reflection) (Fouad et al., 2017), which conclusively depends on surrounding surface reflectivities. Kotak et al. (2015) investigated the effect on a PV façade by using an empirical equation (Liu and Jordan, 1963) to estimate the reflected-energy contribution, recording an increase of 48% in energy gain. Given the consideration of the average albedo of commonly used materials between 0.32 and 0.38, Zhu et al. (2020) used 0.4 as an empirical parameter in the estimation. However, there is still a lack of effective acquisition of reliable building albedo information in the study area.

Except for conducting *situ* investigations to obtain data, early works on material recognition tend to identify textures from close-up pictures without any background (Dana et al., 1999; Fritz et al., 2004; Mallikarjuna et al., 2006). After that, studies start recognizing materials of real-world objects instead of distinguishing close-up textures (Sharan et al., 2014; Bell et al., 2013, 2015). However, most existing material identify methods target on indoor objects. By contrast, urban envelopes materials is typically required to be identified from further distances with blurrier details, a more complex environment, and less discriminating shapes. To reduce the gaps, Xu et al. (2023) proposed a new dataset containing street-level images of Hong Kong and a multi-scale contextual attention network to understand the details and contextual information of façade in complex urban environments. In this study, the development was based on the results of MSCA to acquire reliable albedo information in the study area.

## 3. Materials and methods

This section introduces the details of the evaluation framework that investigates the effect of albedo on solar PV potential distribution. The framework includes the deep learning pipeline which acquires real-world building reflectance information at a large scale, a methodology that converts segmentation output into reflectance and connects them to a 3D model, and the solar irradiation estimation that incorporates multi-reflection.

### 3.1. Evaluation framework

The overall evaluation framework is illustrated in Fig. 1. As shown in Fig. 1(a), this study utilizes a vehicle-based mobile mapping system equipped with the Global Navigation Satellite System (GNSS) and Inertial Measurement Unit (IMU) to capture street views with high-precision geographical coordinates. Then, as depicted in Fig. 1(b), the

street view images are processed using the MSCA, a segmentation network that identifies materials from street-level images on a large scale. In step (c), we employed the Collinearity equation to map the pixels from the image coordinate system to the Hong Kong 1980 Grid System, thereby associating the segmentation results with the 3D model. After identifying all buildings in the study area, different albedo schemes were proposed to evaluate the effects of materials on solar potential.

As shown in Fig. 1(d), the upper row demonstrates a scheme where all façades, regardless of material categories, are assigned a constant albedo. In contrast, the bottom row of (d) illustrates a scheme that assigns different albedos to each material based on the segmentation results. However, due to the limited material categories that MSCA can identify, the third scheme, depicted in the middle row of (d), involves further classification to simulate a more complex urban environment. The initial categories obtained by MSCA are further divided into detailed subclasses. This experiment aims to employ a more comprehensive simulation to understand the multi-reflection in a complex albedo environment.

In Fig. 1(e), the three albedo schemes are applied in parallel to the 3D models to estimate the annual solar potential distribution considering multi-reflection. Based on the estimation results, in step (f), the effects of albedo and other spatial factors (e.g., land utilization, building height, density, and function) are quantified and discussed.

Furthermore, a critical aspect of the methodology lies in its focus on comparative scenario analysis rather than absolute accuracy improvement. This design was necessitated by the complexity of urban solar potential modeling. Long-term validation necessitates not only permanent pyranometer installations but also sustained governmental permissions and calibration efforts. Short-term validation, while operationally feasible, confronts unresolved research gaps: transient weather variability (e.g., cloud cover fluctuations) and unmodeled microclimatic interactions (e.g., dynamic shading from façade protrusions or vegetation) introduce uncertainties that current urban solar models struggle to isolate, particularly when disentangling albedo-specific effects. These limitations echo in the existing studies (Zhu et al., 2020, 2022), whose short-term validation of daily irradiance estimations, with the same 3D framework adopted here, revealed 10%–30% relative errors, surpassing the albedo-induced discrepancies observed in our study (8.0–9.1%). To circumvent these barriers, this study rigorously fixes geometric and meteorological variables while quantifying uncertainties in material recognition (MSCA segmentation) and 3D projection, thereby isolating the albedo's role in redistributing solar irradiation in the following chapters. This design prioritizes mechanistic insights into how albedo assumptions shape district-scale irradiation patterns, avoiding claims of empirical superiority among specific albedo strategies or values.

### 3.2. Study area

To investigate the solar potential distribution in metropolitan cities, this study selected a typical district in Hong Kong as the study area. North Point, located in the Eastern District in the northeastern part of Hong Kong Island, is characterized by its high population density, which results in complex land utilization and heterogeneous façades. As shown in Fig. 2, the eastern portion of North Point is predominantly residential. On-site investigations revealed that residential buildings in this area were typically constructed in the last century, with façades commonly featuring mosaic tiles and paint. In contrast, the western and southern parts of North Point are more multifunctional, comprising residential, commercial, industrial, and a significant proportion of institutional land use. Consequently, the architectural materials in these areas are more varied, including glass, ceramic, and metals, creating a sophisticated environment for estimating solar reflection. Additionally, compared to the high-density downtown area by the seaside, the southern part of North Point is surrounded by woodland. Residential buildings in this area are relatively isolated from one another, resulting in less inter-building reflection, which can serve as a control group for the high-density districts.

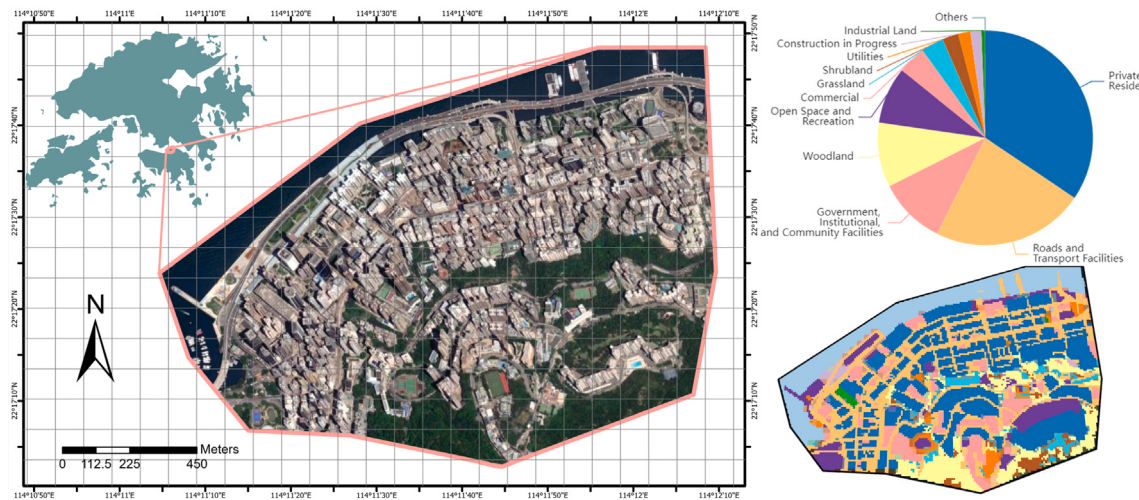


**Fig. 2.** Land utilization and corresponding percentages in the study area(the North Point district of Hong Kong). Land utilization and building types in the study area are used to analyze the influence of solar potential distribution caused by façade albedo.

### 3.3. Façade materials acquiring

To efficiently acquire urban façade material information, this study employs the Multi-Scale Contextual Attention Network (MSCA) proposed in our prior work (Xu et al., 2023). As previously outlined, two assumptions were introduced to streamline the annotation process and manage computational complexity: (1) Each building comprises at most two primary components. This reflects the prevalent architectural styles in Hong Kong, where lower floors often serve commercial functions with distinct materials (e.g., glass), while upper residential sections use materials like ceramic tiles. (2) Each component is dominated by a single material. While real-world façades often feature mixed components and materials (e.g., glass windows embedded in ceramic walls), we prioritize the dominant material to balance annotation feasibility and model accuracy. These assumptions, while pragmatic, inherently limit the model's ability to resolve fine-grained material mixtures. For instance, hybrid façades (e.g., glass-ceramic composites) may be misclassified due to ambiguous material proportions. Nevertheless, our controlled experimental design isolates albedo as the primary variable, ensuring mechanistic insights into its role in solar potential redistribution.

Furthermore, the MSCA architecture, illustrated in Fig. 1, integrates three core components: (1) a High-Resolution Network (HRNet-W48) backbone to preserve fine-grained details from high-resolution street-view imagery; (2) a Multi-Head Attention (MHA) module that projects features into diverse representation subspaces for comprehensive semantic interpretation; and (3) a Multi-Scale Object-Contextual Representation (OCR) block that dynamically fuses contextual information from multiple scales at the feature level. The HRNet backbone processes input images at two scales ( $1.0\times$  and  $0.5\times$ ), balancing pixel-level detail retention and larger receptive field acquisition. The MHA module, configured with eight parallel attention heads, generates preliminary segmentation masks by interpreting hierarchical features across semantic subspaces. These masks are then refined by the Multi-Scale OCR, which computes attention scores between pixel representations (from high-resolution features) and object region contexts (from both scales), enabling the adaptive fusion of fine details and broader contextual patterns. A residual block further optimizes the final output, mitigating gradient degradation while enhancing segmentation precision.

During training, the MSCA network used dual-scale images cropped to  $896 \times 896$  pixels ( $1.0\times$ ) and  $448 \times 448$  pixels ( $0.5\times$ ) from original  $2046 \times 2046$  street views. To ensure computational efficiency, a batch size of 2 per GPU (2x TITAN RTX) was employed, totaling 4 per iteration. The model utilized Stochastic Gradient Descent (SGD) with

momentum (0.9) and weight decay (0.0001), initialized with a learning rate of 0.02 under a linear decay schedule. Cross-entropy loss was applied, with auxiliary losses from preliminary segmentation masks weighted at 0.5 for both scales. Data augmentation strategies, including random horizontal flipping and rotation, were implemented to enhance generalization across diverse urban environments.

Additionally, since the original MSCA is trained on the dataset of North Point street views, which is also the study area for this research, the same pre-trained model and segmentation strategies are used to acquire façade materials. Based on the reflectivity and visual distinguishability of different materials, façades are categorized into ceramic tile, glass, hybrid, metal, mosaic tile, and paint. However, due to the complex reflection characteristics of materials and the limitations of visual identification, the original classification does not fully align with material albedos. Furthermore, the limited identified categories cannot adequately reflect the complex albedo environment in urban areas. Therefore, adjustments and further classifications were made to the segmentation results of MSCA according to the three albedo schemes applied to evaluate the effects of materials on solar potential.

For the segmentation-based scheme, mosaic tile and ceramic tile are merged due to their minor material distinctions, despite significant differences in appearance. Consequently, this scheme includes five classes: ceramic tile, glass, hybrid, metal, and paint. The classification method relies primarily on the segmentation results of MSCA. The MSCA achieved state-of-the-art accuracy in the urban material recognition task (with precision at 0.80, recall at 0.84, and an F1-score of 0.82), demonstrating sufficient precision for district-scale solar potential analysis. While misclassifications persist, particularly for materials with overlapping spectral characteristics (e.g., ceramic and mosaic tiles), the overall accuracy ensures reliable albedo differentiation across dominant façade categories. For solar potential estimation, marginal segmentation errors could translate to localized discrepancies in reflected irradiation. However, our framework reduces systemic biases introduced by uniform albedo assumptions (e.g., constant 0.4), which oversimplify urban reflectance diversity.

Beyond the segmentation-based scheme, this study proposes a further classification to simulate the complex albedo environment in urban areas. As shown in Table 1, excluding glass, the original four materials are subdivided into 29 more detailed categories. Each subcategory is visually distinguishable from the others based on differences in color or roughness. After obtaining the material information from MSCA, the RGB data and segmentation results of each pixel in street views are projected onto the 3D model. To quantify the similarity between the RGB distributions of building façades and reference subclasses in the albedo

**Table 1**

Further classification of façade materials and the characteristics of each subclass.

| Class   | No. | Color      | Description                    |
|---------|-----|------------|--------------------------------|
| Ceramic | C1  | Brown      | Glazed                         |
|         | C2  | Red        | Glazed                         |
|         | C3  | Black      | Smooth                         |
|         | C4  | Gray       | Uneven,new                     |
|         | C5  | Gray       | Granite-like, polished         |
|         | C6  | Gray       | Granite-like, glazed           |
|         | C7  | Red        | Granite-like, glazed           |
|         | C8  | Red        | Granite-like, weathered        |
| Metal   | M1  | Gray       | Paint-sprayed, smooth          |
|         | M2  | Green      | Painted, smooth                |
|         | M3  | Gray       | Aluminum, shiny                |
| Paint   | P1  | Gray       | Concrete                       |
|         | P2  | Gray       | Concrete, porous               |
|         | P3  | Gray       | Concrete, fine roughness       |
|         | P4  | Gray       | Concrete, smooth               |
|         | P5  | Gray       | Painted, smooth                |
|         | P6  | Brown      | Concrete                       |
|         | P7  | Indigo     | Concrete                       |
|         | P8  | Light gray | Concrete                       |
|         | P9  | Bronze     | Concrete                       |
|         | P10 | Cedar      | Concrete                       |
|         | P11 | Dark red   | Concrete                       |
| Hybrid  | H1  | Gray       | Glass-ceramic hybrid, polished |
|         | H2  | Gray       | Glass-ceramic hybrid, glazed   |
|         | H3  | Red        | Glass-ceramic hybrid, glazed   |
|         | H4  | Red        | Glass-ceramic hybrid, smooth   |
|         | H5  | Gray       | Glass-paint hybrid, concrete   |
|         | H6  | Gray       | Glass-paint hybrid, concrete   |
|         | H7  | Gray       | Glass-paint hybrid             |

library, we employed the Jensen–Shannon divergence (JSD). This metric is chosen over alternatives like the Kullback–Leibler (KL) divergence due to its symmetric property, which ensures that the dissimilarity between a façade's RGB distribution  $P_1$  and a reference subclass  $P_2$  is independent of their comparison order, a critical requirement for unbiased material matching. Furthermore, JSD provides a bounded output range  $[0, 1]$ , where 0 indicates identical distributions and 1 maximal dissimilarity. This boundedness allows consistent interpretation of similarity across diverse material categories, unlike the unbounded KL divergence. Additionally, JSD mitigates numerical instability inherent in KL divergence, such as infinite values when encountering zero probabilities in sparse or noisy real-world RGB data, by averaging over a smoothed mixture distribution  $\frac{(P_1+P_2)}{2}$ . The formulation is defined as:

$$JS(P_1 \parallel P_2) = \frac{1}{2} KL(P_1 \parallel \frac{(P_1 + P_2)}{2}) + \frac{1}{2} KL(P_2 \parallel \frac{(P_1 + P_2)}{2}) \quad (1)$$

$$KL(p \parallel q) = \sum_{i=1}^N [p(x_i) \log p(x_i) - p(x_i) \log q(x_i)] \quad (2)$$

where  $KL(\cdot)$  is the Kullback–Leibler divergence.  $P_1$  is the distribution of the building while  $P_2$  corresponds to a reference subclass in the albedo library.

#### 3.4. Data projection

Since the original street view images frequently encounter issues such as overexposure and occlusion, it is necessary to screen out most unqualified images. This makes it challenging to ensure that there are sufficient consecutive photos of each object to accurately identify its location. Therefore, the geographic coordinates of real-world points need to be calculated using a single image. In this study, the Collinearity equation and 3D building models are employed to achieve this objective.

The Collinearity equation describes a straight line formed by the image point, the projection center, and the real-world point. As illus-

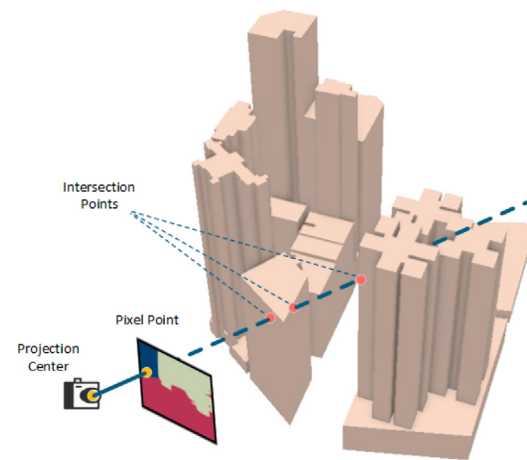


Fig. 3. Using the Collinearity equation to determine the geographic relationship between the camera, street views, and buildings.

**Table 2**  
Projection accuracy evaluation.

| Metrics                                    | Value   |
|--|---------|
| Total points                               | 35      |
| Points projected onto the correct building | 28      |
| Average distance from camera               | 89.19 m |
| RMSE                                       | 3.01 m  |
| Mean error                                 | 2.11 m  |
| Error per meter                            | 0.07 m  |

**Table 3**  
Albedos of common materials in urban areas.

| No. | Material        | Albedo    | Source                        |
|-----|-----------------|-----------|-------------------------------|
| 1   | Light roof      | 0.35–0.5  | Salleh et al. (2014)          |
| 2   | Dark roof       | 0.08–0.18 | Salleh et al. (2014)          |
| 3   | Asphalt ground  | 0.05–0.3  | Yaghoobian and Kleissl (2012) |
| 4   | Concrete façade | 0.17–0.27 | Salleh et al. (2014)          |
| 5   | Brick façade    | 0.2–0.4   | Yaghoobian and Kleissl (2012) |
| 6   | Gypsum façade   | 0.35      | Yaghoobian and Kleissl (2012) |

trated in Fig. 3, given the image point and the projection center, we can obtain a ray pointing to the corresponding geographic point. Based on the occlusion relationship between the camera and the object, the first intersection point determined by the ray and the buildings is the corresponding real-world point.

#### 3.4.1. Accuracy assessment

Given the challenge of validating the mapping across all pixels, 3D model points, and real-world points, this study focused solely on selected feature points to assess the accuracy of the projection pipeline. The feature point in this study, defined as the corner vertices of buildings in street view images, can be readily and accurately matched to their corresponding positions in the 3D model, thereby serving as optimal reference points for evaluating the projection accuracy. However, due to the presence of obstructing buildings and the fixed position of the mapping system, coupled with limitations in camera perspectives, only the central portions of buildings were captured by the camera in most circumstances. Consequently, the number of captured building vertexes is limited, reducing the sample size available for evaluation.

As detailed in Table 2, all 35 feature points were chosen for accuracy evaluation, with 28 correctly projected onto their respective buildings. Among these 28 points, the root mean square error (RMSE) was calculated to be 3.01 m, and the mean error was 2.11 m. It is important to note that most feature points were captured from buildings situated at an average distance of 89.19 m, which exceeds the typical distance of regular points in street views. Consequently, the

**Table 4**  
Material albedo library.

| Library | Size | Including materials   |
|---------|------|---|
| KLUM    | 181  | Asphalt, Brick (clay), Mortar, Ceramic, Concrete, Granite, Limestone, Metal, Plaster, Sandstone, Conglomerate, Wood |
| LUMA    | 74   | Quartzite, Stone, Granite, Asphalt, Cement/Concrete, Brick, Roofing shingle, Roofing tile, Metal, PVC               |
| IGDB    | 5000 | Specular glazing  |
| LBNL    | 87   | Conventional and cool pigmented coatings  |

actual overall error in projection points should be considerably lower than these reported values.

Furthermore, given that the segmentation results are at the building level and albedo assignments are based on the entire building's material distribution, minor misplacements of pixels along building boundaries have minimal impact on the identification of building materials. Therefore, the current level of accuracy in projection is deemed adequate for proceeding with albedo determination in subsequent stages.

### 3.5. Albedo determination

This study employs three methods for assigning façade albedo to evaluate their impacts on solar potential distribution. The first method utilizes a constant albedo to represent all façade materials in urban areas. Based on the research of Salleh et al. (2014), Yaghoobian and Kleissl (2012), the albedos of common materials in urban areas are listed in Table 3. The table indicates that the average albedo ranges between 0.2 and 0.4. Zhu et al. (2020) suggested that simulations achieve optimal performance when the albedo is set to 0.4. Consequently, this study adopts an albedo of 0.4 as an empirical parameter in the constant albedo scheme, which serves as the control group in the experiments.

The second scheme utilizes segmentation results to assign albedos. After merging mosaic tile and ceramic categories, façades are categorized into five groups: ceramic tile, glass, hybrid, metal, and paint. Numerous studies have documented the albedos of these five materials. As shown in Table 4, KLUM (Ilehay et al., 2019) presents an urban spectral library consisting of collected in situ material spectra with imaging spectroscopy techniques in the visible and near-infrared (VNIR) and short-wave infrared (SWIR) spectral range, with 181 façades materials. Similarly, LUMA (Kotthaus et al., 2014) and LBNL (Levinson et al., 2005) present 74 and 87 material spectra, respectively. Specifically, for glass, the International Glazing Database (IGDB) (Versluis et al., 2012) provides more than 5000 optical data for different glasses, including color, reflectance, emissivity, thickness, and so on. Based on the prevalent façades styles in Hong Kong, this study selected several materials from aforementioned libraries to represent the five categories. The albedos of the five categories in this scheme (ceramic, metal, paint, hybrid, glass) are set as 0.14, 0.31, 0.17, 0.28, and 0.13, respectively. The segmentation-based scheme serves as the experimental group for evaluating the effect of façade albedos in different districts.

The third scheme extends the segmentation approach further. Based on preliminary results, façade materials are subdivided into 29 subclasses to simulate the intricate albedo environment in urban settings. This paper selects 29 commonly observed materials in Hong Kong as subclasses. Each building's materials are classified into the specific subclass with the minimum Jensen–Shannon divergence within its initial category. The corresponding albedos for each subclass are detailed in Table 5.

### 3.6. Solar irradiation estimation

To accurately determine solar radiation at specific times and locations, the solar potential estimation follows the 3D urban solar model

established by Zhu et al. (2020), integrating geometric occlusion, multi-reflection, and meteorological parameters. First, hourly solar radiation on horizontal surfaces was computed using the Point Solar Radiation toolbox in ArcGIS Pro (ArcGIS, 2019). Inputs included 1 m-resolution 3D point clouds, latitude ( $22.28^{\circ}$  N for Hong Kong), diffuse proportion, and transmissivity. Among them, the diffuse proportion and transmissivity were calculated through the following formula (Huang et al., 2008):

$$\text{Diffuse} = 0.20P_{\text{clear}} + 0.45P_{\text{partlycloud}} + 0.70P_{\text{cloudy}} \quad (3)$$

$$\text{Transmissivity} = 0.70P_{\text{clear}} + 0.50P_{\text{partlycloud}} + 0.30P_{\text{cloudy}} \quad (4)$$

where  $P_{\text{clear}}$ ,  $P_{\text{partlycloud}}$ , and  $P_{\text{cloudy}}$  represent the proportions of days in clear, partly cloudy, and cloudy conditions, respectively. Cloud cover is one of the most significant factors affecting radiation in this function. The monthly cloud cover data in this study is collected by the Hong Kong Observatory (Observatory, 2024).

The initial horizontal irradiance outputs were then extended to vertical façades by incorporating solar geometry. The solar altitude and azimuth angles were used for each hourly timestep to calculate direct beam exposure across millions of 3D points. This required dynamic shadow detection and occlusion analysis to determine whether neighboring structures shaded a point on a façade or rooftop. The line-of-sight (LOS) between each point and the sun's position was evaluated iteratively, a process demanding hundreds of millions of spatial queries due to the scale of data (over millions of points per study area).

To address this computational intensity, PostgreSQL with the PostGIS extension was employed for optimized spatial operations. Conventional tools like Python or ArcGIS proved inadequate for such large-scale 3D analyses. PostgreSQL enabled efficient R-tree spatial indexing to accelerate occlusion queries and recursive SQL workflows to simulate multi-reflection effects. Radiation paths were tracked iteratively: after each reflection, residual energy was redistributed based on surface albedo until three iterations were completed. Specifically, the choice of three reflection iterations follows (Zhu et al., 2020), where simulations indicated that over 95% of reflected radiation escapes to the sky after multiple reflections. For albedo values of 0.4 and 0.2, residual radiation drops below 7% and 0.8% after three iterations, justifying this threshold for computational efficiency.

The final annual solar potential was derived by accumulating hourly irradiation values across all surfaces. Despite leveraging PostgreSQL's parallel processing capabilities (distributing tasks across 24 computing nodes), the simulations required months to resolve occlusion and reflection effects, underscoring the computational challenges of high-resolution urban solar modeling.

## 4. Experiments

In this section, we provided the setup details and present the experimental results. The experimental results quantitatively evaluate the effect of façade albedo in different types of areas and explore the role of various albedo assignment schemes at different time scales. The findings indicate that the materials of building façades significantly influence the estimated solar irradiation.

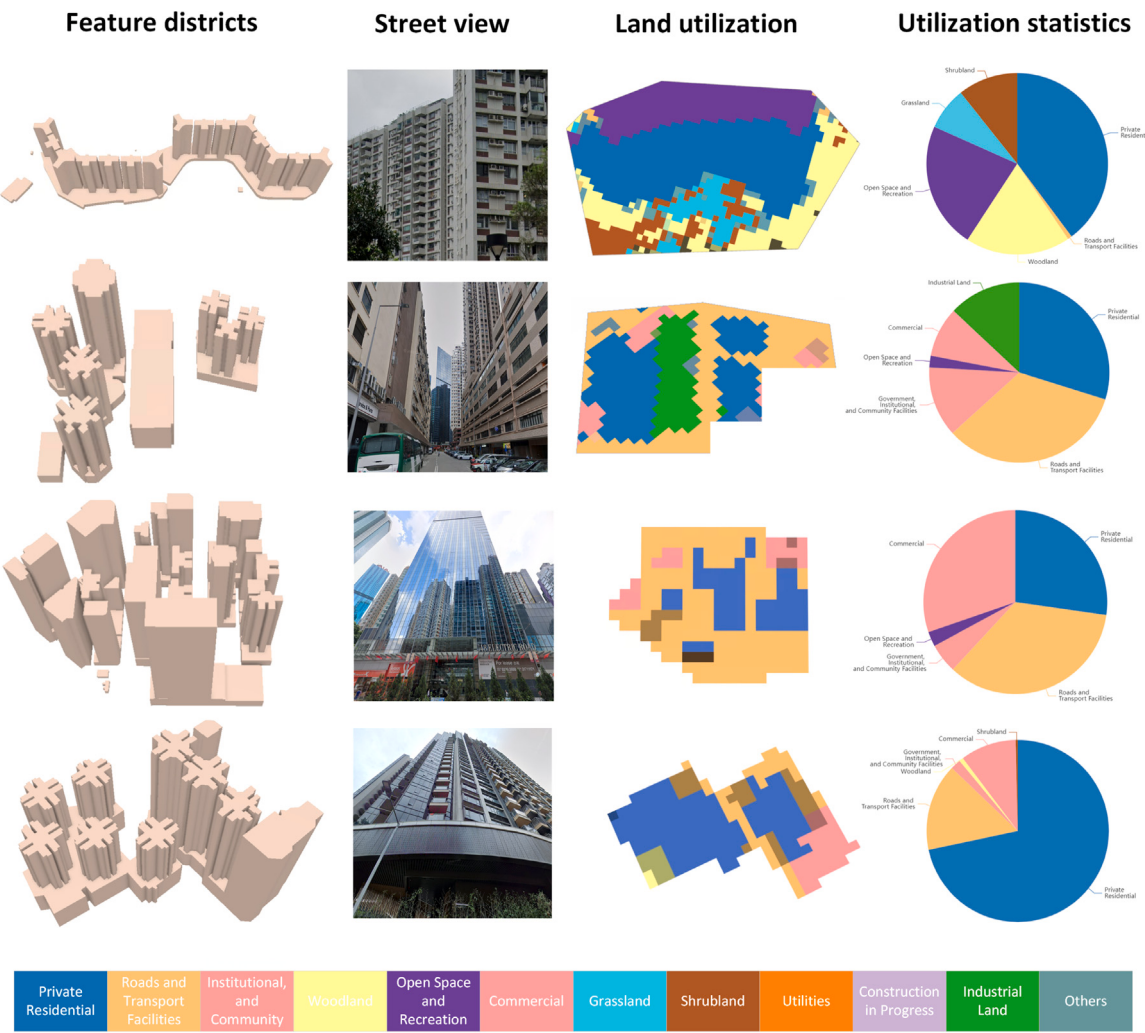


**Fig. 4.** The selected district and corresponding Land utilization in the North Point. The first column on the left is the 3D models of selected districts. The second column is sample street views. The third and fourth columns are the corresponding Land utilization statistics.

**Table 5**  
Assigned albedo of each façade materials.

| Class   | Albedo | Subclass | Albedo | Class | Albedo | Subclass | Albedo | Class  | Albedo | Subclass | Albedo |
|---------|--------|----------|--------|-------|--------|----------|--------|--------|--------|----------|--------|
| Ceramic | 0.14   | C1       | 0.15   | Paint | 0.17   | P1       | 0.26   | Hybrid | 0.28   | H1       | 0.16   |
|         |        | C2       | 0.14   |       |        | P2       | 0.43   |        |        | H2       | 0.28   |
|         |        | C3       | 0.14   |       |        | P3       | 0.51   |        |        | H3       | 0.23   |
|         |        | C4       | 0.35   |       |        | P4       | 0.52   |        |        | H4       | 0.18   |
|         |        | C5       | 0.09   |       |        | P5       | 0.37   |        |        | H5       | 0.24   |
|         |        | C6       | 0.34   |       |        | P6       | 0.04   |        |        | H6       | 0.37   |
|         |        | C7       | 0.23   |       |        | P7       | 0.18   |        |        | H7       | 0.30   |
|         |        | C8       | 0.14   |       |        | P8       | 0.21   |        |        | Glass    | 0.13   |
| Metal   | 0.31   | M1       | 0.31   |       |        | P9       | 0.33   |        |        |          |        |
|         |        | M2       | 0.20   |       |        | P10      | 0.17   |        |        |          |        |
|         |        | M3       | 0.25   |       |        | P11      | 0.12   |        |        |          |        |

#### 4.1. Experimental setups

This study selects North Point as the research area due to its diverse range of building types and façade styles, including fully glazed office buildings, old residential buildings with mosaic tile façades, and factories with painted exteriors. Based on these building styles, the paper specifically chose four distinct neighborhoods for experimental comparison, as illustrated in Fig. 4.

Area 1, depicted in Fig. 4, consists of isolated residential areas with buildings aligned in rows and no adjacent structures nearby. This region serves as a control group to investigate the impact of façade

albedos on solar potential with minimal multi-reflection between buildings. The pie chart on the right of the first row in Fig. 4 shows that, apart from the selected buildings, the majority of this area comprises woodland, open spaces, and grasslands. Correspondingly, as shown in the 'outlying area' of Fig. 5, the façades in this region are relatively homogeneous, predominantly consisting of ceramic tiles.

In contrast, Area 2 is more complex. Located in the northwest corner of North Point, this region includes various types of buildings with different functions and styles, such as private residences, government facilities, factories, and commercial buildings. As shown in Fig. 5, the materials constituting the façades in this region are also more diverse,

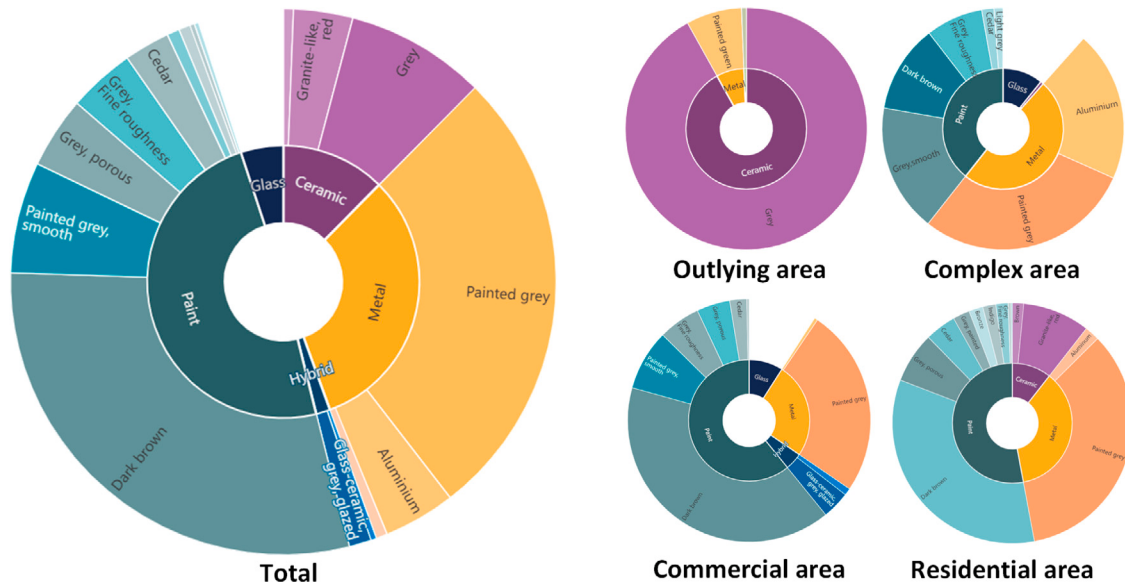


**Fig. 5.** The percentage of different building façade materials in each districts. The inner circle represents the material percentages obtained by the MSCA network. The outer circle represents the material percentages after further classification.

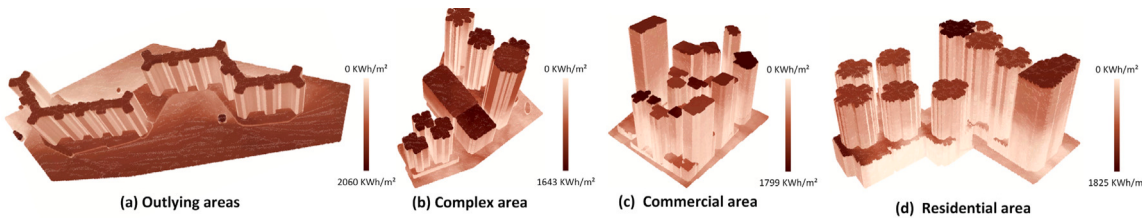


**Fig. 6.** The distribution of annual solar potential across the four study areas under the segmentation-based albedo assignment strategy.

including a significant amount of metal (e.g., aluminum), coatings of various colors, and a substantial proportion of glass façades.

Similarly, Area 3, the commercial area, has a material composition similar to Area 2, with several additional hybrid buildings (e.g., a combination of glass curtain walls and ceramic tiles). Compared to older residential areas, the buildings in Area 3 appear more aesthetically pleasing and modern. Area 4 predominantly consists of residential buildings, differing from Area 3, which is a mix of commercial and residential structures. Furthermore, due to the typical structure of buildings in Hong Kong, the lower floors of these residential buildings in Area 4 are often used for commercial purposes, such as shopping malls, which provide extra diversity in façade albedos. Overall, the selected regions encompass commercial, industrial, and residential buildings with façades made from more than twenty different reflective materials, providing a comprehensive basis for research and analysis.

Additionally, due to the high computational cost associated with a spatial sampling interval of one meter, this experiment conducted temporal sampling at intervals of every 28 days from January 1st to December 31st.

#### 4.2. Estimation based on different albedo schemes

Based on the settings mentioned above, the annual solar potential for the selected study areas under different albedo allocation strategies was determined. As shown in Fig. 6, the distribution of annual solar potential across the four study areas under the segmentation-based albedo assignment strategy is illustrated. The figure reveals that, compared to the vertical surfaces of buildings, the points on horizontal surfaces exhibit higher solar potential across all study areas. This is attributed

to the fact that horizontal surfaces can evenly receive sunlight from east to west throughout the day and experience fewer obstructions, thereby maximizing solar exposure. In contrast to the solar potential distribution at 3 PM on August 13, depicted in Fig. 7 for Area 4, where noticeable solar potential concentration occurs due to reflected sunlight, such phenomena are less apparent in the annual solar potential distribution. This discrepancy arises because the distribution of reflected light varies and is uneven at any specific moment. No particular area is consistently illuminated by reflected solar radiation throughout the day. Even at the same time on different days, variations in the sun's azimuth and altitude angles cause the positions of reflected light from the buildings, which have fixed spatial relationships, to differ. Consequently, the indirect components are unevenly distributed across the study areas on an annual scale. Furthermore, since reflected components do not dominate the overall solar potential distribution, their impact becomes less noticeable in annual-scale visualizations. Fig. 8 further demonstrates that, regardless of the study area or albedo allocation strategy, the proportion of solar potential contributed by direct sunlight consistently ranges between 77% and 90%, constituting the majority of the total solar potential.

However, it does not diminish the role of façade albedo in the total solar potential distribution. Even without considering multiple reflections between buildings, the retained irradiation is still determined by the building's albedo when solar first apart from the architecture. Then, the redistribution of the reflected irradiation is significantly influenced by the interaction between buildings, which is dominated by their spatial relationship and albedos. As shown in Fig. 8, in Area 1, the total solar potential under the simulation albedo scheme is 9.1% higher than that under the constant albedo scheme. In Area 2,



**Fig. 7.** At 3 p.m. on August 13th, the distribution of solar energy potential in Are 4. The purple circle represents the concentration of solar potential caused by the reflection of sunlight.

the segmentation-based scheme results in an 8.0% higher total solar potential compared to the constant scheme. For Area 3, the simulation albedo scheme surpasses the constant scheme by 8.3%, and in Area 4, the segmentation-based scheme exceeds the constant scheme by 8.9%. If multiple reflections are not considered, the differences between various albedo assignment strategies would be even more pronounced. The maximum differences between the different strategies across the regions are 11.9%, 15.6%, 17.8%, and 14.0%, respectively. This is because the albedo strategy, in conjunction with the spatial relationship between buildings and the sun, determines the initial distribution and subsequent redistribution of solar potential.

Specifically, the impact of different façade albedo on solar potential distribution is illustrated in Fig. 9. This figure highlights the differences in annual solar potential distribution resulting from varying façade albedo strategies. Fig. 9(a) compares the annual solar potential under the segmentation-based strategy to that under the constant strategy. The primary differences are observed in the façades, while the rooftops and ground surfaces maintain consistent albedo values. Apart from insignificant visual differences due to multiple reflections, the horizontal surfaces exhibit nearly zero discrepancy. This can be seen from the predominantly purple points on the horizontal surfaces in the image, which indicates negligible differences. Points closer to blue represent negative differences, while points approaching yellow indicate positive differences, with a shift toward yellow signifying more significant differences.

Fig. 9 shows that in Area 1, the outlying area, the differences in solar potential distribution across the three strategies are relatively evenly distributed. This is because Area 1 consists of isolated buildings with minimal obstructions in the north-south direction, providing similar lighting conditions and consistent building materials for façades. As a result, the east-west distribution of buildings has little impact on solar potential. The favorable lighting conditions result in significant and uniform differences in solar potential from the upper to lower levels on the sun-facing sides of buildings. Compared with the distribution under the constant scheme, both the segmentation-based and the simulation schemes believe that based on the façade material of Area 1, in the actual distribution, the façade of this area should exhibit higher solar energy potential. This difference becomes more pronounced with more abundant sunlight.

In addition to the patterns above, other factors also influence the distribution of solar potential in Area 2. As shown in the second, third, and fourth columns of Fig. 9, the differences in solar potential tend

**Table 6**

Detail indicators of each area.

|                           | Area 1  | Area 2 | Area 3 | Area 4 |
|---------------------------|---------|--------|--------|--------|
| Open area/ $m^2$          | 198 131 | 16 007 | 12 522 | 9990   |
| Building footprint/ $m^2$ | 20 705  | 13 974 | 10 242 | 17 126 |
| Open space ratio          | 90.5%   | 53.3%  | 55.0%  | 36.8%  |
| Average height/ $m$       | 65.7    | 72.9   | 74.1   | 91.6   |

**Table 7**

The solar potential ratio of façade to roof in different areas.  $R_{seg}$ ,  $R_c$ , and  $R_{sim}$  represent the ratio under segmentation-based, constant, and simulation strategies, respectively.  $R_{max}$  is the maximum value of  $R_{seg}$ ,  $R_c$ , and  $R_{sim}$  in the study area.  $R_{max} - R_{min}$  serves as an indicator representing the changes in solar distribution caused by changes in albedo.

|            | $R_{seg}$ | $R_c$ | $R_{sim}$ | $R_{max} - R_{min}$ |
|------------|-----------|-------|-----------|---------------------|
| Area 1     | 1.91      | 1.79  | 2.25      | 0.46                |
| Area 1     | 5.42      | 5.08  | 6.39      | 1.30                |
| w/o podium | 2.31      | 1.93  | 2.31      | 0.38                |
| Area 2     | 2.71      | 2.39  | 2.76      | 0.37                |
| Area 3     | 1.82      | 1.58  | 1.82      | 0.25                |
| Area 4     |           |       |           |                     |

to increase with building height. This is because, in the metropolitan environment, the complex spatial layout results in dynamic shading relationships among buildings at different moments. Higher floors are less likely to be shaded, allowing façade areas at these levels to receive better sunlight. As previously noted, better lighting conditions amplify the differences caused by varying albedo values.

However, a different pattern emerges in the second column of Fig. 9(b). In the residential building located at the lower right corner of Area 2, near an industrial-like structure, the solar potential difference initially decreases and then increases from top to bottom on the side facing the factory. This trend is also evident in rows (a) and (c), where the façade shows a similar pattern of weakening and then strengthening differences. This anomaly is difficult to explain by considering only the direct component of irradiation. This variation in solar potential differences can be attributed to reflections from the factory roof and the different absorptivity of irradiation by the façade materials themselves. Due to these indirect components, the lower floors exhibit greater differences in solar potential.

Similarly, the southwest façade of the industrial-like building displays a complex and uneven pattern of differences, with inconsistent trends observed in rows (a) and (b). This suggests that direct irradiation differences are not the dominant factor in this case. Instead, the complexity and heterogeneity of the sources of indirect components play a significant role. Additionally, discrepancies in recognition of the source buildings' materials, which the reflected solars come from, among the three albedo strategies further contribute to the complexity and unevenness of the patterns. Consequently, the heterogeneous nature of the indirect components, combined with the weak direct components, results in the observed complexity and unevenness in the patterns.

#### 4.3. Solar potential distribution influenced by the district morphology

The morphology and function of the study areas significantly influence the distribution of solar potential. As shown in Fig. 4, the four study areas are categorized based on their primary use: outlying residential area, complex area, commercial area, and downtown residential area. Relevant indicators for these areas are listed in Table 6. Undoubtedly, building height, density, and façade orientation significantly affect the amount of accessible radiation. However, in this section, we mainly focus on the impact of albedo differences caused by morphology and function on the distribution of solar potential.

Firstly, Areas 1 and 4 are primarily residential. Within the selected regions, these residences are likely from the same developer or built in the same period, resulting in consistent building heights and styles. In high-density urban environments, similar heights mean rooftops are

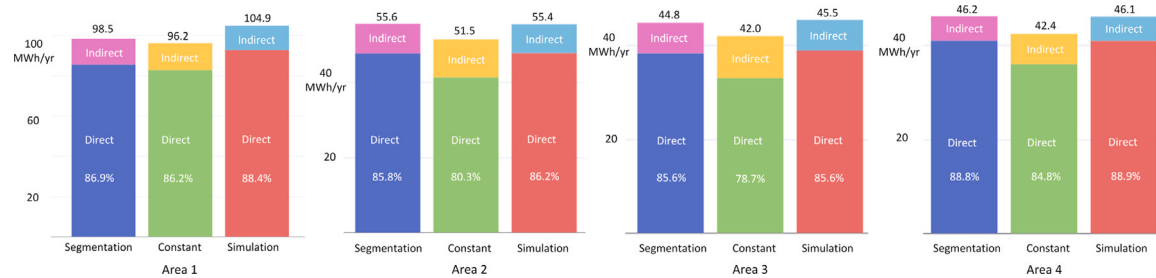


**Fig. 8.** Comparison of the total annual solar potential of each study area under different albedo assignment strategies. ‘Direct’ refers to the part of solar irradiation that comes from direct sunlight. ‘Indirect’ represents the indirect components.

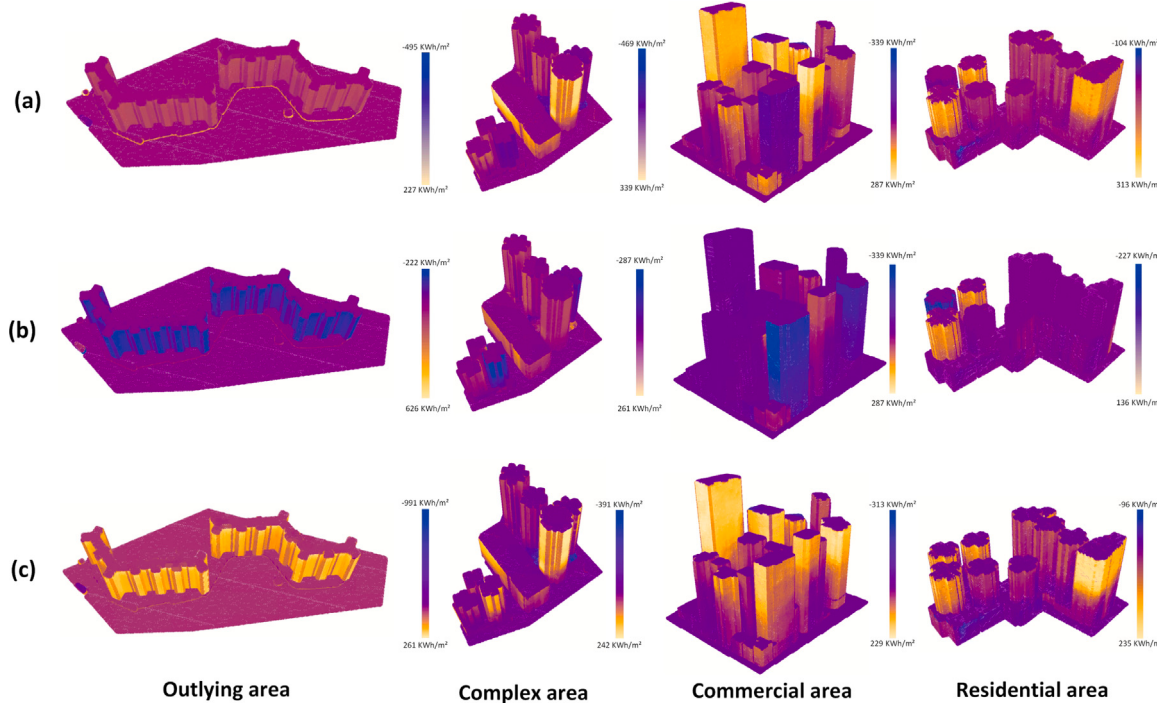


**Fig. 9.** Differences in façade albedo impact the distribution of annual solar potential across four study areas. (a) shows the annual solar potential under the segmentation-based strategy minus that under the constant strategy. (b) represents the solar potential under the segmentation-based strategy minus that under the simulation strategy. (c) illustrates the difference between the simulation and constant strategies.

less likely to be shaded, while façades are more likely to be shaded. In such areas, the solar potential of the façade accounts for a more significant proportion of the total distribution. Consequently, as shown in Table 7, compared to Areas 2 and 3, which are also in the downtown area, Area 4 has the lowest  $R$  values (1.82, 1.58, and 1.81 under the three albedo allocation strategies) despite having the highest average building height of 91.6 m.

In contrast, the situation differs in suburban areas. Due to the lack of obstructions (after excluding a large podium area from Area 1 rooftop statistics), the extensive façade area results in a considerable  $R$  value. Under the segmentation-based, constant, and simulation albedo strategies, the  $R$  values reach 5.42, 5.08, and 6.39, respectively. Simultaneously, the impact of façade material albedo on solar potential distribution is greatest in Area 1, with the difference between  $R_{sim}$  and  $R_c$  reaching 1.31, compared to a maximum difference of 0.38 in other areas. As described in Table 7, in this context,  $R_{max} - R_{min}$  can serve as an indicator for observing the changes in solar distribution caused by changes in albedo.

Area 2, in contrast, is more inclined to be multifunctional, with more architectural styles and larger differences in building heights. The situation is similar in the commercial area. Compared with the homogeneous residential building, it is difficult to ensure that the

office buildings in a commercial area are built in the same period and maintain the same height, which results in significant portions of rooftop areas frequently being shaded. Thus, although the average heights of Areas 2 and 3 (72.9 m and 74.1 m, respectively) are lower than Area 4 (91.6 m), their  $R$  values are higher.

Moreover, the diversity in building types and uses leads to heterogeneous façade albedos. This diversity allows us to observe more significant changes in the distribution of solar potential when the façade albedo shifts from the constant to the simulation strategy in Areas 2 and 3, with changes of 0.38 and 0.37, respectively, both higher than the 0.25 observed in the urban residential area.

#### 4.4. Albedo-caused effects under different temporal scales

##### 4.4.1. Intra-annual scale

Throughout different seasons, even at the same clock, the solar elevation angle and incident angles vary. The unequal daylight duration across seasons also results in a non-uniform annual distribution of solar potential. For example, in Area 4, as illustrated in Fig. 10, solar potential in the first and fourth quarters is significantly lower than in the second and third quarters.

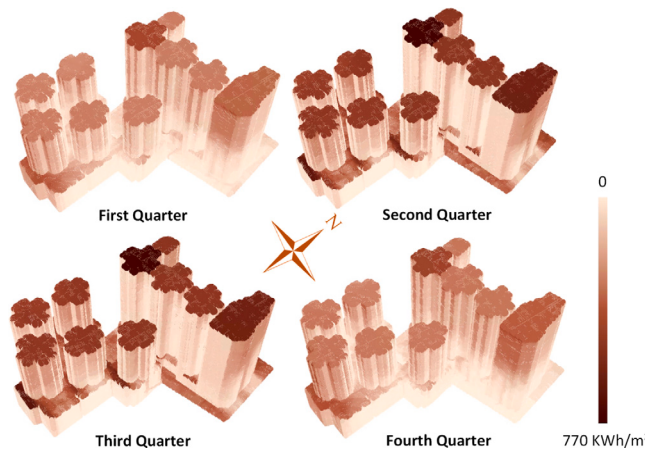


**Fig. 10.** Distribution of solar potential in different quarters for Area 4 under segmentation-based scheme.

**Table 8**

The solar potential ratio of façade to roof in Area 4 under different quarters.

|           | $R_{seg}$ | $R_c$ | $R_{sim}$ | $R_{max} - R_{min}$ |
|-----------|-----------|-------|-----------|---------------------|
| Quarter 1 | 2.66      | 2.33  | 2.66      | 0.34                |
| Quarter 2 | 1.31      | 1.11  | 1.30      | 0.20                |
| Quarter 3 | 1.32      | 1.11  | 1.30      | 0.20                |
| Quarter 4 | 2.83      | 2.47  | 2.83      | 0.36                |

Due to the study area standing near  $22.28^\circ$  N, the sun reaches its highest elevation angle during the summer. A higher solar elevation angle means that building façades are less likely to be shaded, exposing a larger surface area to sunlight. This is evident in Fig. 10, where, during the second and third quarters, the red areas on the rightmost building, indicative of strong solar irradiation, extend to lower floors. However, factors beyond the elevation angle also influence the illuminated area. In the first and fourth quarters, sunlight predominantly impacts the south-facing sides of buildings, while in summer and autumn, the north-facing sides receive more sunlight. This means the projection area of buildings in different azimuths also determines the illuminated surface area. Unlike the commercial area's rectangular buildings with high aspect ratios, the residential buildings have nearly circular cross-sections, ensuring a relatively consistent illuminated area throughout the year.

Despite minimal changes due to azimuth angles, the increased elevation angle still enhances the illuminated façade area. However, in Fig. 10, the façade colors remain relatively consistent across all four quarters, with only the illuminated surface varying. This consistency occurs because the higher solar elevation angle reduces the angle of incidence on the façades, thereby decreasing the component of irradiation projected perpendicularly onto the façade. Consequently, the overall irradiation intensity on the façades does not significantly vary across the seasons.

In contrast, the solar potential on horizontal surfaces shows significant seasonal variations. Both rooftops and ground surfaces receive irradiation primarily influenced by the solar elevation angle and daylight duration. In the second and third quarters, when the elevation angle is higher, horizontal surfaces exhibit markedly greater solar potential. Considering both the façade and horizontal surfaces, the results in Table 8 can be derived. During winter and spring, the  $R$  values in the study area are relatively high, reaching up to 2.66 and 2.83, respectively. In these seasons, differences in façade albedo significantly impact the overall solar potential distribution, with  $R_{max} - R_{min}$  values reaching 0.34 and 0.36.

**Table 9**

The solar potential ratio of façade to roof in Area 3 under different hours.

|           | $R_{seg}$ | $R_c$ | $R_{sim}$ | $R_{max} - R_{min}$ |
|-----------|-----------|-------|-----------|---------------------|
| Morning   | 3.95      | 3.54  | 4.06      | 0.51                |
| Noon      | 1.93      | 1.68  | 1.96      | 0.27                |
| Afternoon | 5.28      | 4.63  | 5.37      | 0.74                |

#### 4.4.2. Hourly scale

Compared to the distribution of solar potential over longer time scales, the hourly distribution within a single day is influenced by more factors and thus exhibits greater variability. The most significant influence is the weather. In Hong Kong, typhoons and heavy rains are common, especially in summer, leading to discrepancies when calculating diffuse proportions, transmissivity, and comparing sampled results. To mitigate the impact of these factors on the hourly solar distribution, data from morning, noon, and afternoon throughout the year were collected and analyzed.

The experiment divided the daytime sunshine into three time periods: morning, noon, and evening, according to the two time nodes (11 a.m. and 2 p.m.). After minimizing the impact of weather, the solar potential distribution within the study area is primarily influenced by geometric factors such as building layout and spatial relationship with the sun. Similar to the results on the seasonal scale, the potential distribution in the study area shows a strong correlation with the solar elevation angle. As illustrated in Fig. 11, taking Area 3 as an example, the elevation angle is the largest at noon, and the sunshine also reaches its peak. Consequently, the overall solar potential of the study area is increased, especially in the horizontal roof and ground areas. Fig. 11 reveals that in the morning and afternoon, the maximum solar potential on horizontal surfaces is comparable to that on façades. However, at noon, there is a noticeable color difference between these surfaces (rooftops appear dark red, while façades are merely orange-red). This phenomenon is also observed in Table 9, where the  $R_{sim}$  value decreases from 4.06 in the morning to 1.96 at noon and rises back to 5.37 in the afternoon. This indicates that horizontal surfaces benefit more from the increased solar elevation. On the contrary, as the elevation angle decreases, the irradiance received by horizontal surfaces drops sharply. This means that the solar potential is more concentrated on the façades during morning and afternoon periods. This is further evidenced by the morning and afternoon  $R_{max} - R_{min}$  values, where 0.74 and 0.51 reflect that selecting different façade albedo strategies during these times will significantly impact the solar potential distribution.

## 5. Discussion and conclusion

This study proposes a comprehensive evaluation modeling framework to quantitatively assess the impact of urban façade albedo on solar potential distribution. The framework includes a deep learning network for efficiently acquiring large-scale urban building façade information, a projection method for converting single, discontinuous 2D images into 3D models, three albedo distribution strategies, and a methodology for quantitatively evaluating the impact of façade albedo on solar potential distribution.

Experimental results indicate that in the selected study area of Hong Kong, different albedo distribution strategies significantly affect the overall solar potential by 8.0% to 9.1%. If multiple reflection effects within buildings are disregarded, the impact can reach 11.9% to 17.8%. Furthermore, after comparing and analyzing different morphological study areas, the experiments observed that buildings with a high open space ratio (e.g., suburban isolated residential areas) are more susceptible to the influence of façade materials on solar potential distribution. In contrast, in metropolitan downtown areas, mixed-use regions and commercial districts with diverse building styles and functions are more affected by façade albedo than residential areas that have more

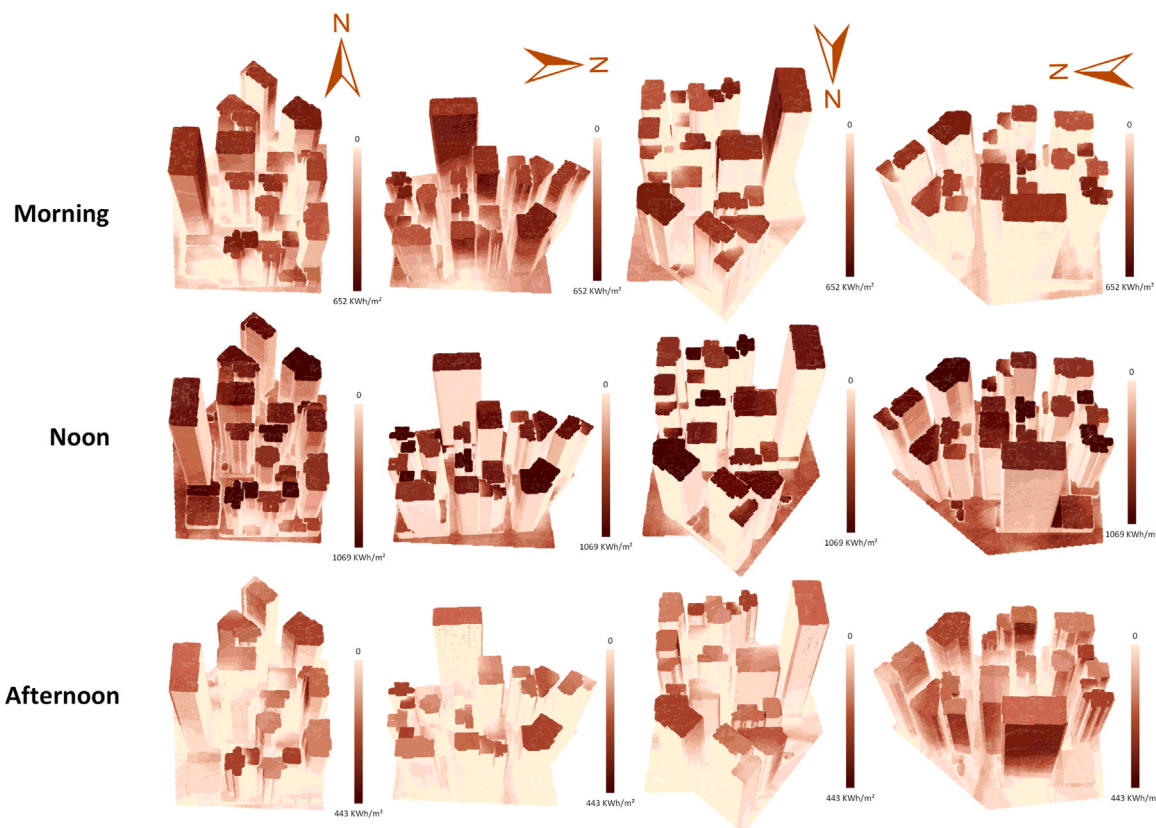


**Fig. 11.** The distribution of solar potential in Area 3 at different time periods throughout the day. The four columns of images represent views of the study area in different orientations.

consistent architectural styles. Additionally, the study compares the distributions across different time scales, observing that during the first and fourth quarters, horizontal surfaces (e.g., rooftops and ground) in the study area receive weaker irradiation, making the differences in façade reflectance more influential on overall distribution changes. On shorter time scales, after mitigating incidental factors (e.g., weather), solar potential distribution in the morning and afternoon is more dependent on façade albedo values for similar reasons.

Efficiently acquiring information on urban façade albedos has long been a domain gap in the research field. The simulation of reflected light remains the most challenging part of indirect solar radiation estimation. Ignoring reflected solar radiation or using a constant albedo to represent the entire city is a typical solution that can introduce considerable inaccuracies. This work addresses this research gap by quantitatively analyzing and discussing how façade materials influence solar potential distribution in modern urban environments, thereby obtaining a better understanding of the relationship between urban morphology and solar capacity by incorporating precise albedo values of urban envelopes (i.e., rooftops, façades, and ground) in simulations.

However, there are still limitations to this study. The urban façade material database established for training the deep learning network contains an insufficient variety and number of building types, particularly in capturing fine-grained architectural elements such as balconies, recesses, or surface-mounted advertisements, which may alter albedo and reflection patterns locally. These omissions stem from data availability and annotation challenges: street-level imagery inherently struggles with occlusions and resolution constraints, while manual labeling of complex façade articulations remains labor-intensive. Additionally, our current framework does not explicitly account for the effects of highly reflective materials (e.g., specular glass or polished metals), which may introduce nonlinear reflectance behaviors not fully

captured by simplified albedo assumptions. The computational demands of high-resolution 3D modeling further limited our analysis to four representative districts, reducing the generalizability of findings across diverse urban morphologies. Addressing these gaps will require future integration of advanced techniques, such as semi-automated annotation pipelines leveraging weakly supervised learning to scale material recognition datasets, or hybrid models combining LiDAR-derived geometric details with street-view imagery to resolve fine-scale façade articulations. Furthermore, expanding the material library to include reflective surface properties and validating against multi-sensor reflectance measurements could enhance the physical fidelity of solar potential simulations. While our work establishes a critical foundation for material-aware urban solar estimation, these limitations underscore the need for interdisciplinary collaboration to bridge computational feasibility and real-world architectural complexity.

To conclude, this study provides a method for accurately simulating urban solar potential distribution by utilizing street view images to extensively acquire building façade information and quantitatively assess the impact of façade reflectance on it. The experimental results enhance our understanding of the relationship between urban morphology and solar capacity.

#### CRediT authorship contribution statement

**Fan Xu:** Writing – review & editing, Writing – original draft, Visualization, Validation, Software, Methodology, Investigation, Formal analysis, Data curation, Conceptualization. **Man Sing Wong:** Supervision, Project administration, Funding acquisition, Conceptualization. **Rui Zhu:** Writing – review & editing, Supervision, Methodology, Conceptualization. **Ying Dang:** Visualization, Software.

## Declaration of competing interest

The authors declare that they have no known competing financial interests or personal relationships that could have appeared to influence the work reported in this paper.

## Acknowledgments

The authors would like to thank the Hong Kong SAR Government departments including the LandsD (for providing the GIS data), HyD (for providing the MMS data), CEDD (for providing airborne LiDAR data).

## Fundings

This project is substantially funded by the General Research Fund (Grant Nos. 15603923 and 15609421), Collaborative Research Fund (Grant No. C5062-21GF) and Young Collaborate Research Fund (Grant No. C6003-22Y) from the Research Grants Council of Hong Kong. The authors acknowledge the funding support (Grant No. BBG2 and CD81) from the Research Institute for Sustainable Urban Development, Research Institute for Land and Space, the Hong Kong Polytechnic University, Kowloon, Hong Kong, China.

## References

- Äğbulut, Ü., Gürel, A.E., Biçen, Y., 2021. Prediction of daily global solar radiation using different machine learning algorithms: Evaluation and comparison. *Renew. Sustain. Energy Rev.* 135, 110114.
- An, Y., Chen, T., Shi, L., Heng, C.K., Fan, J., 2023. Solar energy potential using GIS-based urban residential environmental data: A case study of Shenzhen, China. *Sustain. Cities Soc.* 93, 104547.
- ArcGIS, 2019. Points Solar Radiation. <http://desktop.arcgis.com/en/arcmap/10.3/tools/spatial-analyst-toolbox/points-solar-radiation.htm>.
- Assouline, D., Mohajeri, N., Scartezzini, J.L., 2015. A machine learning methodology for estimating roof-top photovoltaic solar energy potential in Switzerland. In: Proceedings of International Conference CISBAT 2015 Future Buildings and Districts Sustainability from Nano To Urban Scale. (CONF), LESO-PB, EPFL, pp. 555–560.
- Assouline, D., Mohajeri, N., Scartezzini, J.L., 2017. Quantifying rooftop photovoltaic solar energy potential: A machine learning approach. *Sol. Energy* 141, 278–296.
- Bell, S., Upchurch, P., Snavely, N., Bala, K., 2013. OpenSurfaces: A richly annotated catalog of surface appearance. *ACM Trans. Graph.* 32 (4), 1–17.
- Bell, S., Upchurch, P., Snavely, N., Bala, K., 2015. Material recognition in the wild with the materials in context database. In: Proceedings of the IEEE Conference on Computer Vision and Pattern Recognition. pp. 3479–3487.
- Besharat, F., Dehghan, A.A., Faghih, A.R., 2013. Empirical models for estimating global solar radiation: A review and case study. *Renew. Sustain. Energy Rev.* 21, 798–821.
- Bill, A., Mohajeri, N., Scartezzini, J.L., 2016. 3D model for solar energy potential on buildings from urban LiDAR data.. In: UDMV. pp. 51–56.
- Boccalatte, A., Fossa, M., Ménézo, C., 2020. Best arrangement of BIPV surfaces for future NZEB districts while considering urban heat island effects and the reduction of reflected radiation from solar façades. *Renew. Energy* 160, 686–697.
- Chen, J.L., He, L., Yang, H., Ma, M., Chen, Q., Wu, S.J., Xiao, Z.I., 2019. Empirical models for estimating monthly global solar radiation: A most comprehensive review and comparative case study in China. *Renew. Sustain. Energy Rev.* 108, 91–111.
- Dana, K.J., Van Ginneken, B., Nayar, S.K., Koenderink, J.J., 1999. Reflectance and texture of real-world surfaces. *ACM Trans. Graph.* 18 (1), 1–34.
- Erdélyi, R., Wang, Y., Guo, W., Hanna, E., Colantuono, G., 2014. Three-dimensional solar radiation model (SORAM) and its application to 3-D urban planning. *Sol. Energy* 101, 63–73.
- Fouad, M., Shihata, L.A., Morgan, E.I., 2017. An integrated review of factors influencing the performance of photovoltaic panels. *Renew. Sustain. Energy Rev.* 80, 1499–1511.
- Freitas, S., Catita, C., Redweik, P., Brito, M.C., 2015. Modelling solar potential in the urban environment: State-of-the-art review. *Renew. Sustain. Energy Rev.* 41, 915–931.
- Fritz, M., Hayman, E., Caputo, B., Eklundh, J.-O., 2004. The Kth-Tips Database. Citeseer.
- Gassar, A.A.A., Cha, S.H., 2021. Review of geographic information systems-based rooftop solar photovoltaic potential estimation approaches at urban scales. *Appl. Energy* 291, 116817.
- Huang, S., Rich, P.M., Crabtree, R.L., Potter, C.S., Fu, P., 2008. Modeling monthly near-surface air temperature from solar radiation and lapse rate: Application over complex terrain in yellowstone national park. *Phys. Geogr.* 29 (2), 158–178.
- Ibrahim, I.A., Khatib, T., 2017. A novel hybrid model for hourly global solar radiation prediction using random forests technique and firefly algorithm. *Energy Convers. Manage.* 138, 413–425.
- IEA, 2023. Renewable energy market update. <https://www.iea.org/reports/renewable-energy-market-update-june-2023>.
- Ilehag, R., Schenk, A., Huang, Y., Hinz, S., 2019. KLUM: An urban VNIR and SWIR spectral library consisting of building materials. *Remote. Sens.* 11 (18), 2149.
- Izquierdo, S., Montañés, C., Dopazo, C., Fueyo, N., 2011. Roof-top solar energy potential under performance-based building energy codes: The case of Spain. *Sol. Energy* 85 (1), 208–213.
- Jiang, H., Dong, Y., Xiao, L., 2017. A multi-stage intelligent approach based on an ensemble of two-way interaction model for forecasting the global horizontal radiation of India. *Energy Convers. Manage.* 137, 142–154.
- Kotak, Y., Gul, M., Munee, T., Ivanova, S., 2015. Investigating the impact of ground albedo on the performance of PV systems.
- Kothaus, S., Smith, T.E., Wooster, M.J., Grimmond, C., 2014. Derivation of an urban materials spectral library through emittance and reflectance spectroscopy. *ISPRS J. Photogramm. Remote Sens.* 94, 194–212.
- Levinson, R., Berdahl, P., Akbari, H., 2005. Solar spectral optical properties of pigments—Part II: Survey of common colorants. *Sol. Energy Mater. Sol. Cells* 89 (4), 351–389.
- Li, Y., Ding, D., Liu, C., Wang, C., 2016. A pixel-based approach to estimation of solar energy potential on building roofs. *Energy Build.* 129, 563–573.
- Liu, B.Y., Jordan, R.C., 1963. The long-term average performance of flat-plate solar-energy collectors: with design data for the US, its outlying possessions and Canada. *Sol. Energy* 7 (2), 53–74.
- Makade, R.G., Chakrabarti, S., Jamil, B., 2019. Prediction of global solar radiation using a single empirical model for diversified locations across India. *Urban Clim.* 29, 100492.
- Mallikarjuna, P., Targhi, A.T., Fritz, M., Hayman, E., Caputo, B., Eklundh, J.O., 2006. The kth-tips2 database. *Comput. Vis. Act. Percept. Lab. Stock. Swed.* 11.
- Meenal, R., Selvakumar, A.I., 2016. Estimation of global solar radiation using sunshine duration and temperature in chennai. In: 2016 International Conference on Emerging Trends in Engineering, Technology and Science. ICETETS, IEEE, pp. 1–6.
- Meenal, R., Selvakumar, A.I., 2018. Assessment of SVM, empirical and ANN based solar radiation prediction models with most influencing input parameters. *Renew. Energy* 121, 324–343.
- Mehaoud, K., Lartigue, B., 2019. Influence of a reflective glass façade on surrounding microclimate and building cooling load: Case of an office building in algiers. *Sustain. Cities Soc.* 46, 101443.
- Nguyen, H.T., Pearce, J.M., 2013. Automated quantification of solar photovoltaic potential in cities overview: A new method to determine a city's solar electric potential by analysis of a distribution feeder given the solar exposure and orientation of rooftops.. *Int. Rev. Spat. Plan. Sustain. Dev.* 1 (1), 49–60.
- Nwokolo, S.C., Obiwulu, A.U., Ogbulezie, J.C., 2023. Machine learning and analytical model hybridization to assess the impact of climate change on solar PV energy production. *Phys. Chem. Earth, Parts A/ B/ C* 130, 103389.
- Observatory, H.K., 2024. Daily mean amount of cloud. [https://www.hko.gov.hk/sc/abouthko/opendata\\_intro.htm](https://www.hko.gov.hk/sc/abouthko/opendata_intro.htm).
- Park, S., Kim, Y., Ferrier, N.J., Collis, S.M., Sankaran, R., Beckman, P.H., 2021. Prediction of solar irradiance and photovoltaic solar energy product based on cloud coverage estimation using machine learning methods. *Atmosphere* 12 (3), 395.
- Quej, V.H., Almorox, J., Ibrakhimov, M., Saito, L., 2016. Empirical models for estimating daily global solar radiation in yucatán peninsula, Mexico. *Energy Convers. Manage.* 110, 448–456.
- Redweik, P., Catita, C., Brito, M., 2013. Solar energy potential on roofs and facades in an urban landscape. *Sol. Energy* 97, 332–341.
- Salleh, S., Latif, Z.A., Pradhan, B., Wan Mohd, W., Chan, A., 2014. Functional relation of land surface albedo with climatological variables: a review on remote sensing techniques and recent research developments. *Geocarto Int.* 29 (2), 147–163.
- Sánchez, E., Izard, J., 2015. Performance of photovoltaics in non-optimal orientations: An experimental study. *Energy Build.* 87, 211–219.
- Sharan, L., Rosenholtz, R., Adelson, E.H., 2014. Accuracy and speed of material categorization in real-world images. *J. Vis.* 14 (9), 12–12.
- Versluis, R., Powles, R., Yazdanian, M., Rubin, M., Jonsson, J., 2012. International Glazing Database: Data File Format. Citeseer.
- Walch, A., Castello, R., Mohajeri, N., Scartezzini, J.L., 2020. Big data mining for the estimation of hourly rooftop photovoltaic potential and its uncertainty. *Appl. Energy* 262, 114404.
- Willenborg, B., Pültz, M., Kolbe, T.H., 2018a. Integration of semantic 3D city models and 3D mesh models for accuracy improvements of solar potential analyses. *Int. Arch. Photogramm. Remote. Sens. Spat. Inf. Sci.* 42, 223–230.
- Willenborg, B., Sindram, M., Kolbe, T.H., 2018b. Applications of 3D city models for a better understanding of the built environment. In: Trends in Spatial Analysis and Modelling: Decision-Support and Planning Strategies. Springer, pp. 167–191.
- Xu, S., Huang, Z., Wang, J., Mendis, T., Huang, J., 2019. Evaluation of photovoltaic potential by urban block typology: A case study of Wuhan, China. *Renew. Energy Focus*, 29, 141–147.
- Xu, F., Wong, M.S., Zhu, R., Heo, J., Shi, G., 2023. Semantic segmentation of urban building surface materials using multi-scale contextual attention network. *ISPRS J. Photogramm. Remote Sens.* 202, 158–168.

- Yaghoobian, N., Kleissl, J., 2012. Effect of reflective pavements on building energy use. *Urban Clim.* 2, 25–42.
- Zhu, R., Kondor, D., Cheng, C., Zhang, X., Santi, P., Wong, M.S., Ratti, C., 2022. Solar photovoltaic generation for charging shared electric scooters. *Appl. Energy* 313, 118728.
- Zhu, R., Kwan, M.P., Perera, A., Fan, H., Yang, B., Chen, B., Chen, M., Qian, Z., Zhang, H., Zhang, X., et al., 2023. Giscience can facilitate the development of solar cities for energy transition. *Adv. Appl. Energy* 100129.
- Zhu, R., Wong, M.S., You, L., Santi, P., Nichol, J., Ho, H.C., Lu, L., Ratti, C., 2020. The effect of urban morphology on the solar capacity of three-dimensional cities. *Renew. Energy* 153, 1111–1126.
- Zhu, R., You, L., Santi, P., Wong, M.S., Ratti, C., 2019. Solar accessibility in developing cities: A case study in Kowloon east, Hong Kong. *Sustain. Cities Soc.* 51, 101738.